In situ atomic force microscopy studies on lithium (de)intercalation-induced morphology changes in Li$_x$CoO$_2$ micro-machined thin film electrodes[☆]

Jonghyun Park [a,*], Sergiy Kalnaus [b], Sangwoo Han [a], Yoon Koo Lee [a], Gregory B. Less [a], Nancy J. Dudney [b], Claus Daniel [b,c,d], Ann Marie Sastry [a]

[a] *Department of Mechanical Engineering, University of Michigan Ann Arbor, 2350 Hayward Street, Michigan, MI 48109-2125, USA*
[b] *Materials Science and Technology Division, Oak Ridge National Laboratory, One Bethel Valley Road, P.O. Box 2008, MS-6083, Oak Ridge, TN 37831-6083, USA*
[c] *Energy and Transportation Science Division, Oak Ridge National Laboratory, One Bethel Valley Road, P.O. Box 2008, MS-6472, Oak Ridge, TN 37831-6472, USA*
[d] *Bredesen Center for Interdisciplinary Research and Education, University of Tennessee, Knoxville, TN 37996-2200, USA*

HIGHLIGHTS

► Conduct a unique *in situ* AFM measurement on micro-machined sample.
► Exclude secondary/non-active materials and remove vagueness due to irregular geometry.
► Develop and validate a proposed coupled electrochemical and mechanical model.
► Reveal the key effects of geometry and kinetics on active material stability.

ABSTRACT

Structural instability due to intercalation-induced stresses in electrode materials is one of the key degradation mechanisms of Li-ion batteries. Fragmentation of material degrades structural integrity and electrical resistance, and also accelerates harmful side reactions. *In situ* experiments are the appropriate approach for investigating the actual time-dependent nature of the behavior changes of an electrode material while it is charged and discharged. In the current work, a unique *in situ* electrochemical atomic force microscopy (ECAFM) measurement is made on samples of cylindrical shape, which are micro-machined by focused ion beam (FIB) microscopy. This pre-defined geometry allows the exclusion of secondary, non-active materials from the electrochemically active material as well as the removal of any vagueness owing from the irregular geometry of particles. The experimental results are also used to validate a proposed coupled electrochemical and mechanical model for determining the stress–strain state of active electrode material during electrochemical cycling. The results produced using this model correlate strongly with the experimental data. The combined results reveal the key effects of the geometry, kinetics, and mechanics of electrode materials on the stress–strain state, which acts as a barometer of the structural stability of a material.

© 2012 Elsevier B.V. All rights reserved.

1. Introduction

LiCoO$_2$ in bulk powder form has been commonly used as a cathode material for commercial Li-ion batteries in consumer electronics since 1990 [1]. For increased safety in large-scale batteries for electric vehicles and grid-scale storage, other derivates of LiCoO$_2$ are used [2,3]. Due to this history in consumer electronics and the large body of associated research, the electrochemical behavior of LiCoO$_2$ is well known and therefore a perfect candidate for developing and testing new characterization methods in association with theory. We selected this material for characterization by a new electrochemical atomic force microscopy method.

Thin films for use as cathode materials have been fabricated by diverse methods including e-beam evaporation [4], pulsed laser ablation [5], sputtering [6], and electrostatic spray deposition [7]. Generally, upon deposition of the thin film, the cathode is annealed

above 700 °C to improve its crystallinity [8–10]. The LiCoO$_2$ thin film has a rhombohedral structure consisting of layers of close-packed networks of oxygen ions separated by alternating layers of Li and Co ions. The hexagonal cell has lattice parameters of $a = 2.815$ Å and $c = 14.05$ Å [11].

During cell cycling, anisotropic structural changes occur as Li-ions (de)intercalate through the active materials. X-ray diffraction measurement has observed the change of lattice spacing in Li$_x$CoO$_2$ as a function of x, where the change in the c-axis is much greater than that in the a-axis. The spacing change in the c-axis increases during charging, reaching a maximum at around $x = 0.5$, after which it decreases. Increasing electrostatic repulsion between CoO$_2$ layers due to deintercalation causes the c-axis lattice parameter to expand by 2.4% from $c = 14.08$ Å in Li$_{0.99}$Co$_{1.01}$O$_2$ to $c = 14.42$ Å in Li$_{0.49}$Co$_{1.01}$O$_2$; the a-axis only shrinks by 0.34% from $a = 2.816$ Å in Li$_{0.99}$Co$_{1.01}$O$_2$ to $a = 2.807$ Å in Li$_{0.49}$Co$_{1.01}$O$_2$ [12]. These changes have been confirmed by several *in situ* and *ex situ* X-ray powder diffraction experiments [13–15].

Structural instability in the form of micro-cracks caused by cycling-induced changes in the lattice parameters has been proposed as a major cause of performance degradation in LiCoO$_2$ batteries. These micro-cracks can lead to fragmentation of the particles, which can affect the particle network and electrical resistance, as well as accelerate side reactions with the electrolyte. A TEM examination of LiCoO$_2$ cathodes cycled between 2.5 V and 4.35 against a Li anode [16] has shown that a significant fraction of the particles was severely strained, fractured, and possessive of a high density of extended defects. Similar damage may be responsible for degradation in the long-term cycling of LiCoO$_2$ Li-ion batteries. Dislocations in LiCoO$_2$ were observed by transmission electron microscopy [17]. It was found that the configurations of all dislocations are glissile and indicative of active slip planes. These glissile dislocations might suggest possible damage mechanisms during cycling.

While pulverized particles have been observed in cycled material, investigation into changes in stress–strain state and damage accumulation as a time-dependent phenomenon is still under way. Experimentally, such works require *in situ* techniques, which impose certain challenges on the design of the experimental setup. The Acoustic Emission (AE) method has been employed to register acoustic waves emitted from the composite Si electrode when fracture occurs during charge and discharge [18]. Recently, nano-mechanical quantification of the elastic, plastic, and fracture properties of LiCoO$_2$ was examined by measuring the Young's elastic modulus, hardness, and fracture toughness [19]. Further, design criteria for electrochemical, shock-resistant battery electrode were made based on the analytical model and *in situ* acoustic emission experiments [20].

While this technique allows for the quantification of freshly produced cracks at each particular time interval, the measurement of strains in the material with the purpose of understanding the constitutive electrochemical–mechanical behavior is limited. *In situ* X-ray experiments provide information on strain and phase transformations in cathode materials [21–23]; however, the technique focuses on the atomistic scale and cannot give a detailed analysis of the electrode scale. Use of Scanning Probe Microscopy (SPM) techniques, on the other hand, enables the observation and collection of data with rather high resolution on a nano-meter scale. While early SPM experiments targeted observation of the overall roughness change in the electrode during electrochemical cycling [24], the technique has been further developed to probe diffusion-induced strains in small features on thin film Li ion battery cathodes [25,26]. *In situ* AFM measurement for roughness of sputter-deposited Si–Sn thin films for electrode material has been conducted [24]. An *in situ* electrochemical AFM measurement was

conducted to study surface and dimensional changes of individual Li$_x$CoO$_2$ crystals during lithium deintercalation [27]. The extent of expansion measured along the c_{hex} axis corresponded with previous X-ray powder diffraction results.

Though previous work has attempted to monitor changes in lattice parameters or surface roughness during intercalation/deintercalation, the results were obscured by the effects of particle geometry and particle size. As previously mentioned, lattice expansion in Li$_x$CoO$_2$ is a function of state of charge [28], which means that stresses due to volume changes result from a concentration of Li-ions in the cathode particles. Depending on the geometry and the size of the particles being measured, the concentration profile changes significantly. Furthermore, a bulk composite cathode includes additive particles such as carbon black particles and PVdF binders [28]. These additive materials may affect the stress level in active particles by changing the boundary conditions. To date, there has been no attempt to measure the strain on an electrode of pre-defined geometry where the shape and volume changes can be observed and measured accurately without being hindered by the presence of additive materials.

In addition, it is nearly impossible to maintain a sample in a perfectly level position during scanned probe measurements on nanometer-scale geometries. Even a small amount of tilt can adversely affect the accuracy of the results. Also, the AFM image is a result of the interaction of the tip shape with the surface topography; the curvature and tip sidewall angles affect the image. For these reasons, the obtained image may need to be processed for the sake of better visual effect or to eliminate measurement error. Here, a well-defined geometry is a benefit because correction is easier than in the case of randomly-shaped geometry.

Modeling efforts on a particle level have been based on the analogy between thermal stresses and stresses introduced by the diffusion of a chemical species into a material [29–35]. A model utilizing binary diffusion coefficients has been developed and used to compute the stresses in LiMn$_2$O$_4$ [36] and carbonaceous material [37]. The thermal analogy-based modeling has been extended from a single particle to a composite electrode [38], and the stress state produced by lithiation was used as an input for the fracture mechanics analysis of an existing crack in active material particles [39,40]. The description of volumetric expansion due to intercalation based on equations of thermal expansion is rather appealing due to the simplicity of the elastic equations, and this approach is adopted in the current investigation by considering electrochemical interactions between the electrode micro-specimen and the electrolyte.

In the present investigation, a micro-specimen of pre-defined geometry was fabricated and an *in situ* AFM technique was applied to measure the morphology changes in this sample during charging and discharging. A Focused Ion Beam (FIB) microscope was used to mill a cylindrical sample out of a LiCoO$_2$ thin film electrode. Simultaneously, a mechanical–electrochemical model including thermodynamics, electrode kinetics, and transport phenomena was developed; this model was used to simulate the same configuration as that in the experiment.

The present work thus attempts to confirm the mechanism that correlates structural instability with capacity fade in Li$_x$CoO$_2$ electrodes. This work focuses on examining the surface morphology evolution of a Li$_x$CoO$_2$ thin film electrode via *in situ* AFM measurement of a micro-electrode and microscale electrochemical modeling. In this study, we have the following objectives:

1. Conduct an *in situ* AFM study to measure morphology changes of a pre-defined thin film based micro-electrode as a function of state of charge, specimen size, and potential sweep rate.
2. Develop a multiphysics-based model for calculating the volume expansion and deformation due to intercalation

considering the multiphase interaction between the electrode and the electrolyte.

3. Compare the simulation results with measurement results and further extend the prediction of mechanical characteristics of the specimen during (de)intercalation, which cannot be measured.

2. Experiments

2.1. Synthesis of LiCoO₂ thin film electrode and micro-machining process using FIB

Thin film samples were prepared by radio frequency magnetron sputtering of a cold-pressed and sintered $LiCoO_2$ target. The substrate consisted of polished 99.6% Alumina with a 300 nm thick gold film deposited as a current collector. In order to improve adhesion of Au to the substrate, a 20 nm thin layer of Ni was deposited first. $LiCoO_2$ was deposited at an average deposition rate of 18 Å min⁻¹, to a final thickness of 2 μm. The samples were annealed at 700 °C for 2 h under a flow of oxygen.

Fabrication of the micro-specimens was performed in a dual beam-focused ion beam/electron beam microscope (Hitachi NB5000). The described procedure yielded thin films with rather low surface roughness and small grain size (about 50–70 nm) of $LiCoO_2$. As a result, no surface deposition of carbon or tungsten was necessary in order to achieve smooth surfaces on the milled pillars. In order to minimize the implantation of the Ga ions into the surface layer of the material, fabrication was performed with decreasing current in each run (ranging from 3.79 nA to 0.07 nA in the final polishing step). The fabrication was monitored with SEM in order to make sure the sample remained attached to the current collector. A thin film with a FIB-fabricated micro-pillar produced in this manner is shown in Fig. 1.

2.2. Electrochemical measurement

The voltage profile of $Li/LiCoO_2$ to be used as a reference in *in situ* AFM measurements was obtained from a thin film sample cycled in a Swagelok cell. The cell was assembled in an argon-filled glove box with H_2O maintained at less than 1 ppm. The cell consisted of a $LiCoO_2$ thin film cathode electrode, a lithium foil anode electrode, and a polypropylene separator (Celgard 2500). The electrolyte solution consisted of 1 M $LiPF_6$ in an 1:1 v/v mixture of ethylene carbonate (EC) and dimethyl carbonate (DMC). The Swagelok cell was allowed to rest overnight in the glove box after assembly prior to cycling. The initial formation cycle was conducted at a rate of C/10 between 3.0 and 4.5 V versus lithium using a Bio-Logic VMP3 potentiostat.

2.3. In situ AFM measurement

In situ AFM experiments for the morphology evolution of the samples were conducted with a Bruker-Nano Multimode AFM with a Nanoscope III controller coupled with a BioLogic VMP3 cycler. The AFM, sitting on a vibration isolator, was located inside an argon-filled glove box, with only the controller and the potentiostat located outside the glove box. The half cell was assembled using a Bruker-Nano MMTEC AFM Fluid cell inside the glove box.

A schematic diagram of the AFM Fluid cell cross-sectional configuration is shown in Fig. 2. Lithium foil, used for the counter electrode, was placed on top of a copper current collector. The AFM Fluid cell was placed on top of the working electrode, and the rim was sealed with a silicone O-ring. The sample was placed in the center below the silicon nitride AFM scanning tip (SNL, Bruker-Nano Probes). Finally, the electrolyte was injected from the right inlet port with the excess exiting from the left inlet as shown in Fig. 2.

To study the time-dependent morphology changes in the particle, cyclic voltammetry was employed. A linearly changing ramp voltage was applied to the electrode. The rate of potential change (sweep rate) was set at two values, 0.39 mV s⁻¹ and 0.78 mV s⁻¹. While the half-cell was potentiodynamically controlled, *in situ* AFM images were collected in contact mode with a non-conductive silicon nitride tip. The stiffness of the tip was 0.58 N m⁻¹ and the radius was 10 nm. Fig. 1 shows an SEM image of a specimen. This specimen has four pillars and one reference at the center of the specimen where the $LiCoO_2$ thin film was removed by FIB, exposing the Alumina substrate. To capture the volume change of the sample at a specific voltage, the scanning was done quickly over a small area. It was found that side reactions such as gas generation and oxidative decomposition of the electrolyte significantly reduce the image quality, further necessitating quick scanning. Consequently, the minimum area required to make visible the effects of shape change was selected. The maximum scan height was 5 μm in the z-direction, and the scanning area was 8.75 μm × 35 μm. The previously mentioned reference point on the samples was included to correct for any drift that might occur in the sample image during data acquisition. Taking all limitations into account, the area selected for AFM imaging included pillar no. 3 (3.8 μm in radius), pillar no. 2 (2.05 μm in radius), and the reference, as marked with the dotted rectangular box in Fig. 1. One AFM image example is shown at the top-left in Fig. 1.
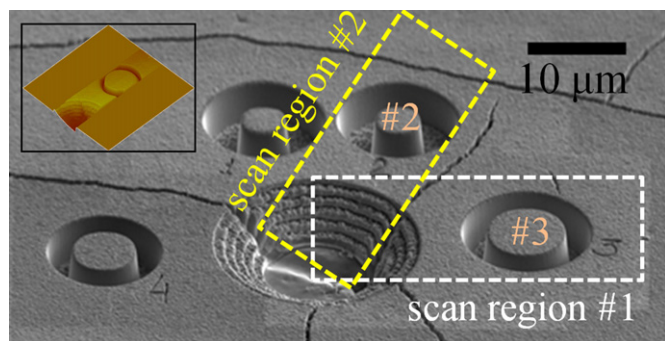

Fig. 1. SEM image of the specimen including four pillars. A larger pillar (no. 3, $r_0 = 3.8$ μm) and a smaller pillar (no. 2, $r_0 = 2.05$ μm) are selected for quick scanning, and are marked with the dotted area. One AFM example is shown in the top-left corner.
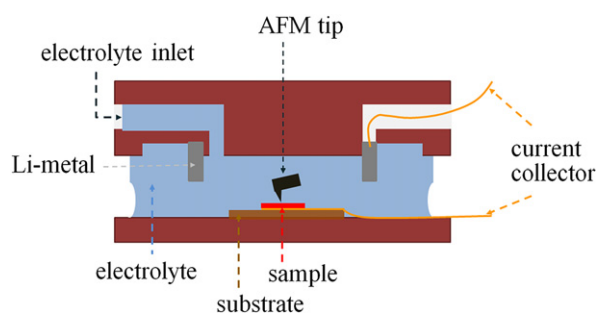

Fig. 2. A schematic diagram of the AFM fluid cell cross-section configuration. The $LiCoO_2$ thin film electrode sits on a bottom-insulated substrate. An aluminum current collector is located between the thin film and the substrate. Lithium metal wire is attached to a copper current collector.

2.4. Image post-processing

The obtained image was processed to correct for the tilt of the sample, which appeared to be inevitable and might have introduced errors if not appropriately treated. As can be seen in Fig. 3, the tilted plane has an angle of θ with the horizontal plane. For the correction, we assumed that the plane was tilted down and away from the upper right corner of the specimen as viewed in Fig. 3. The constants in the equation for the tilted plane, $z = ax + by + c$, were found based on least-mean-squares fitting, after which the cross line and the angle between two planes ($z = ax + by + c$ and $z = 0$) were calculated. In order to perform the correction, the tilted plane was rotated around the cross line between the two planes. After rotating the tilted plane through the cross line passing a point $\mathbf{A}$ with a direction vector $\mathbf{U}$ by an angle θ, the new position, $\mathbf{X}'$ (located in the horizontal plane of a point $\mathbf{X}$ in the tilted plane), can be calculated from the product of sequential rotation matrices:

$$\mathbf{X}' = \left[\mathbf{A} + \frac{(\mathbf{X} - \mathbf{A})\cdot\mathbf{U}}{|\mathbf{U}|^2}\mathbf{U} \right] (1 - \cos\theta) + \cos\theta\mathbf{X} + \frac{1}{|\mathbf{U}|}\mathbf{U}$$
$$\times (\mathbf{X} - \mathbf{A})\sin\theta \tag{1}$$

Fig. 4 shows one example of a post-processed result where (a) is the obtained image and (b) is the cross section of the obtained image showing the tilt. Fig. 4c and d shows the corrected image after rotating the image, where the tilt has been corrected.

3. Numerical simulations

3.1. Description of the modeling

Mapping of the Li-ion concentration inside the electrode microsample is necessary for tracking the morphology change of the sample and for determining strain in the micro-pillar. In addition, the Li-ion concentration in the electrolyte around the micro-pillar is needed to determine the kinetics associated with the reaction at the interface between the specimen and the electrolyte. This means that a diffusion-only model of the Li-ion in the solid particle, as assumed in the previous work [41], is insufficient for capturing the exact phenomena at the interface between the particle and the electrolyte. At the interface of the lithium metal and the electrolyte, Li-ions are dissociated from or reduced into the lithium metal during the discharge–charge processes as:
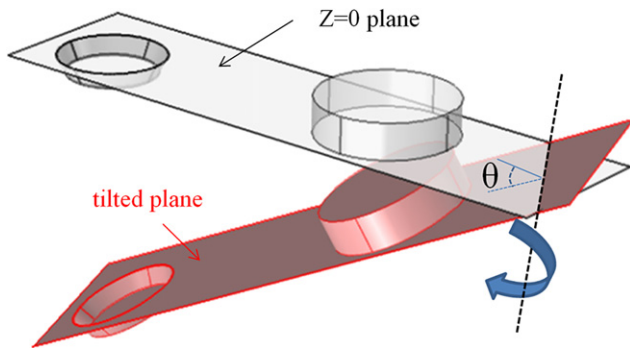
$$\text{Li} \underset{\text{charge}}{\overset{\text{discharge}}{\rightleftharpoons}} \text{Li}^+ + e^- \tag{2}$$

Fig. 3. A schematic diagram of a tilted plane (measured plane) and horizontal plane (correction target plane). The angle between the two planes is θ and those two planes share a cross line. The tilted plane is rotated about the cross line by angle θ to correct the image.
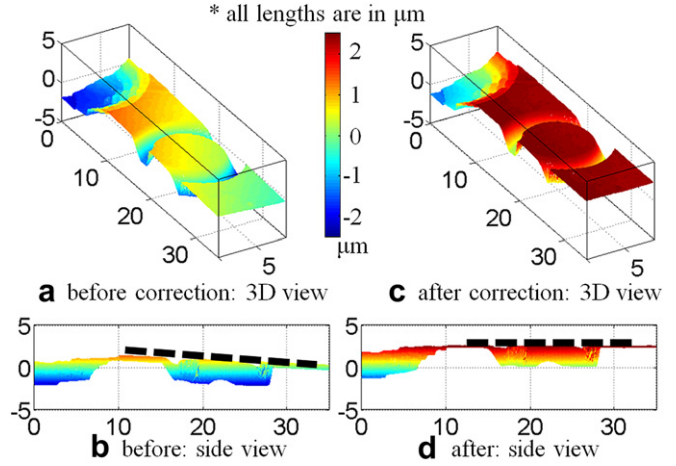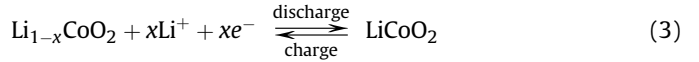

Fig. 4. One example of post-processing. The original image and corrected images are shown as indicated: (a) the original 3D image, (b) the original cross section image, (c) the corrected 3D image, and (d) the corrected cross section image.

Similarly, the redox phenomenon occurs at the interface between Li_xCoO_2 and the electrolyte as expressed below:

$$\text{Li}_{1-x}\text{CoO}_2 + x\text{Li}^+ + xe^- \underset{\text{charge}}{\overset{\text{discharge}}{\rightleftharpoons}} \text{LiCoO}_2 \tag{3}$$

The rate of the reactions represented by Eqs. (1) and (2) can be modeled by the Butler–Volmer equation:

$$j_i^{\text{Li}} = i_0 \left(\exp\left(\frac{\alpha_a F}{RT}\eta_i\right) - \exp\left(-\frac{\alpha_c F}{RT}\eta_i\right) \right) \tag{4}$$

where i_0 is the exchange current density, α_a, α_c are anodic and cathodic transfer coefficients for the electrode, respectively, R is the gas constant, F is the Faraday's constant, and T is the temperature. Here, η_i stands for the surface overpotential defined as

$$\eta_i = \phi_i - \phi_e - U_i \tag{5}$$

where φ_i, φ_e are the surface potentials at the interface of the electrode ($i = 1$ for the anode and $i = 2$ for the cathode) and the electrolyte, and U_i is the open circuit potential. The exchange current density determines the rate of the reaction and depends upon the reactant and product concentration adjacent to the interface as follows:

$$i_0 = k(c_s)^{\alpha_c}(c_s^{\max} - c_s)^{\alpha_a}(c_e)^{\alpha_a} \tag{6}$$

where c_s and c_e represent Li-ion concentration at the particle surface and in the electrolyte, $c_s^{\max}$ stands for the maximum surface concentration, and k is the reaction rate constant.

The governing equations for the electrodes and the electrolyte involve charge conservation in the solid (Eq. (7) in S-domain in Fig. 5) and the electrolyte (Eq. (8) in E-domain in Fig. 5) and mass transport law in the solid (Eq. (9) in S-domain in Fig. 5) and the electrolyte (Eq. (10) in E-domain in Fig. 5):

$$\nabla\cdot(\sigma\nabla\phi_s) = 0 \tag{7}$$

$$\nabla\cdot\left(-\kappa\nabla\phi_e - \frac{\kappa RT}{F}\left(1 + \frac{\partial\ln f}{\partial\ln c_e}\right)\left(1 - t_+^0\right)\nabla\ln c_e \right) = 0 \tag{8}$$

$$\frac{\partial c_s}{\partial t} + \nabla\cdot\left[-D_s\left(\nabla c_s + \frac{\Omega c_s}{RT}\nabla\sigma_h\right) \right] = 0 \tag{9}$$
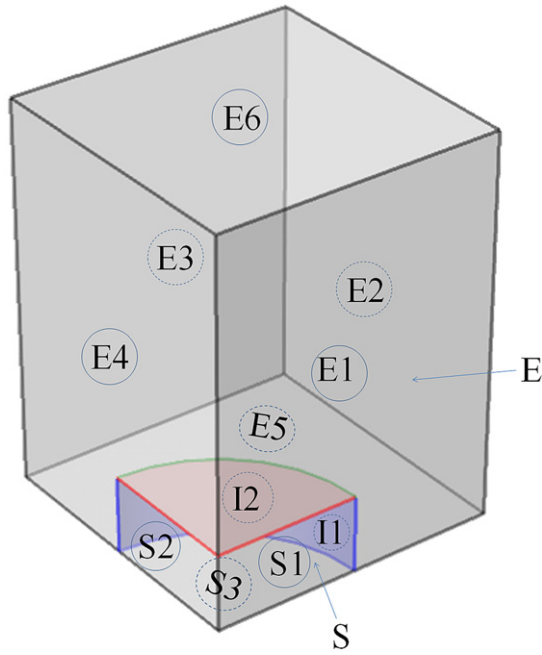
Fig. 5. A schematic of a half-cell and model representation. ¼ Geometry was employed using symmetric boundary conditions. 'S' and 'E' represent the solid and the electrolyte, respectively. 'I' stands for interface between the two phases.

$$\frac{\partial c_e}{\partial t} + \nabla \cdot (-D_e \nabla c_e) + \frac{i \cdot \nabla t_+^0}{F} = 0 \tag{10}$$

where σ is the conductivity of the solid particle, ϕ_s is potential in the solid particle, κ is ionic conductivity in the electrolyte, ϕ_e is the potential in the electrolyte, f is the mean molar activity coefficient, t_+^0 is the cation transference number, D_s is the diffusion coefficient in the solid, Ω is the partial molar volume, σ_h is hydrostatic stress, D_e is the diffusion coefficient in the electrolyte, and i is the current density in the electrolytic solution.

In Eq. (9), the first term in the flux term accounts for the effect of the concentration gradient, where lithium ions diffuse to lower concentration regions from higher concentration regions. The second term accounts for the effect of the stress gradient. This effect originates from the fact that an intercalated lithium ion displaces the host atoms and sets up a strain field in the host structure. Since this strain field affects the energy of a second intercalated ion, this leads to an elastic interaction between the two ions.

The stress–strain relation, including the effect of the intercalation-induced strain, is given by:

$$\varepsilon_{ij} = \frac{1}{E}\left[(1+v)\sigma_{ij} - v\sigma_{kk}\delta_{ij}\right] + \frac{\tilde{c}\Omega}{3}\delta_{ij} \tag{11}$$

where ε_{ij}, σ_{ij} are strain and stress components, kk represents summation notation, E is Young's modulus, v is Poisson's ratio, $\tilde{c} = c - c_0$ is the lithium ion concentration change from the stress-free state, and δ_{ij} is the Kronecker delta. The last term accounts for the intercalation strain. Note that Eqs. (9) and (11) are coupled through the concentration c and the hydrostatic stress σ_h.

3.2. Initial boundary conditions and material properties

The equations above were given the following initial boundary conditions:

For the electronic current balance in the solid particle expressed by Eq. (7):

$$-\mathbf{n}\cdot\mathbf{\Gamma} = -j_i^{Li}\Big|_{I1,I2}, \quad -\mathbf{n}\cdot\mathbf{\Gamma} = -j_i^{Li}\Big|_{S1,S2}, \quad \phi_s = \phi_{app}\Big|_{S3} \tag{12}$$

For the charge balance in the electrolyte expressed by Eq. (8):

$$-\mathbf{n}\cdot\mathbf{\Gamma} = 0\Big|_{E1 \sim E5}, \quad -\mathbf{n}\cdot\mathbf{\Gamma} = j_i^{Li}\Big|_{I1,I2,E6} \tag{13}$$

For the material balance in the solid expressed by Eq. (9):

$$-\mathbf{n}\cdot\mathbf{\Gamma} = 0\Big|_{S1 \sim S3}, \quad -\mathbf{n}\cdot\mathbf{\Gamma} = -j_i^{Li}\Big/F\Big|_{I1,I2} \tag{14}$$

For the mass transport law in the electrolyte expressed in Eq. (10):

$$-\mathbf{n}\cdot\mathbf{\Gamma} = 0\Big|_{E1 \sim E5}, \quad -\mathbf{n}\cdot\mathbf{\Gamma} = j_i^{Li}\Big/F\Big|_{I1,I2,E6} \tag{15}$$

where $\mathbf{n}$ and $\mathbf{\Gamma}$ represent the normal vector and flux vector, respectively. For the solid mechanics calculation, roller conditions were applied to the symmetric plane (S1 and S2), and the bottom surface (S3) was fixed. The outer surfaces were given no constraint. Uniform initial conditions are assumed, i.e., $c_e = c_e^0$, $c_s = c_s^0$, $\phi_s = \phi_s^0$, $\phi_e = \phi_e^0$. The list of the parameters used in the simulation is provided in Table 1. Solution of the system of differential equations was performed by the Finite Element Method using COMSOL software.

4. Results and discussion

The annealed thin films of LiCoO$_2$ were analyzed by X-ray diffraction using a PANalytical X'Pert Pro system with a molybdenum source ($\lambda = 0.709319$ Å). Rietveld refinement was done using X-pert High Score Plus software. The calculated lattice constants were $a = b = 2.8143$ Å and $c = 14.030$ Å, which were in accordance with previously reported results for LiCoO$_2$ single crystals [42] and synthesized powders [43]. Fig. 6 shows the diffraction pattern of the thin film in the 2-theta range containing the three principal diffraction lines (003), (101), and (104). The film showed (104) preferred orientation (46%). With the (104) plane parallel to the substrate, the c-axis makes a 350° angle with respect to the substrate plane, which provides access to the lithium layers for faster Li ion diffusion as compared to the case where the c-axis is perpendicular to the substrate.

Fig. 7 shows the voltage profile of a cell in a Swagelok assembly with a constant current charge/discharge. The voltage profile showed a plateau at around 3.9 V, which corresponds to the Li$_{0.94}$CoO$_2$ semiconductor to Li$_{0.75}$CoO$_2$ metal transition. This data was used as a reference for the *in situ* AFM measurements. One example of the AFM image is shown at the top left in Fig. 1, where the scanned regions are at the center of the figure, and the two outer flat planes represent unscanned regions. These AFM images were used to determine the height changes of the micro-pillars. Fig. 8 shows the average heights of the center areas (340 nm × 340 nm) of pillars no. 3 ($r_0 = 3.8$ μm) and no. 2 ($r_0 = 2.05$ μm) shown in Fig. 1 while the applied potential was swept at a rate of 0.39 mV s^{-1}. The solid blue line represents simulation results at the center point of pillar no. 3, and the dotted red line represents simulation results at the center point of pillar no. 2. The blue circle bar marked 'x' indicates the experimental measurements at the center point of pillar no. 3, and the unmarked red circle bar indicates the experimental measurements at the center point of pillar no. 2. As seen in Fig. 1, the surfaces of the machined pillars show roughness due to multigrain boundaries. As Li-ions are removed from the layered structure, the volume expansion will vary depending on the grain orientation. The

Table 1
Values of parameters used in the simulations.

Parameters	LiCoO$_2$	Ref.
LiCoO$_2$ particle properties		
D (mol m^{-3})	1×10^{-13}	[38]
σ (S m^{-1})	10	[38]
E (GPa)	70	[38]
ρ (kg m^{-3})	5030	[38]
Ω (m^3 mol^{-1})	7.35×10^{-7}	[42,45–49]
v	0.2	[38]
Interface interaction properties		
Cathode		
α_a, α_c	0.5, 0.5	[50]
k (A m$^{-2}\cdot$	1.27×10^{-6}	[38]
(mol m^{-3})$^{-1.5}$)		
i_0 (A m^{-2})	85.0 (anode only)	[51]
Electrolyte properties		
D_2 (m^2 s^{-1})	7.5×10^{-11}	[50]
κ (S m^{-1})	$2.602 \times 10^{-2} + 5.877 \times 10^{-4}c_e - 9.946 \times$	[50]
	$10^{-7}c_e^2 + 1.435 \times 10^{-10}c_e^3 - 1.387 \times 10^{-14}c_e^4$	
Constants		
R (J·(mol K)$^{-1}$)	8.314	
T (K)	$273.15 + 25$	
F (C mol^{-1})	96,487	
Initial and boundary values		
c_e^0 (mol m^{-3})	1000	
c_s^0 (mol m^{-3})	$0.98C_{max}$	
ϕ_s^0 (V)	3.9 V	
ϕ_e^0 (V)	0	

maximum difference can be as much as 50 nm when the c-axis expands by 2.4% at the same time that the a-axis shrinks by 0.34%; if the initial roughness is taken into consideration, this variance can be increased further. In Fig. 8, and in subsequent figures showing the experimentally obtained height change, the vertical bars serve to reflect the surface roughness. The half-range of these bars represents one standard deviation from the mean value based on the measurements of height change over the scanned area.

In order to observe the height change upon delithiation (charge) as a function of voltage in the *in situ* AFM cell, the average value is compared to the simulation result. The initial voltage in the simulation was set to 3.9 V. In the fluid cell, polarization may increase due to the ohmic resistance across the electrolyte where the distance between the reference and working electrode is longer
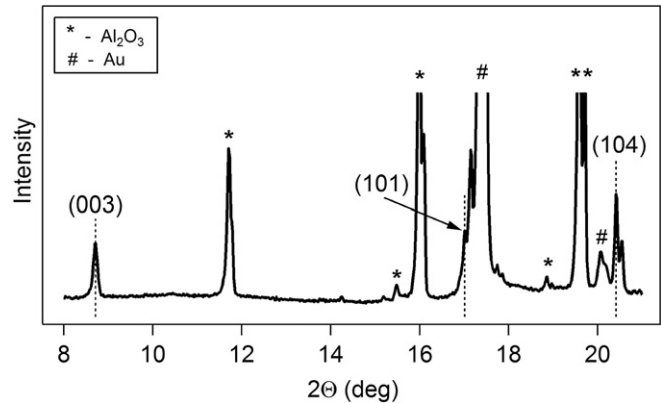

Fig. 6. XRD pattern of the LiCoO$_2$ thin film. Al$_2$O$_3$ peaks (*) and Au peaks (#) originate from the substrate and current collector supporting the LiCoO$_2$ thin film.
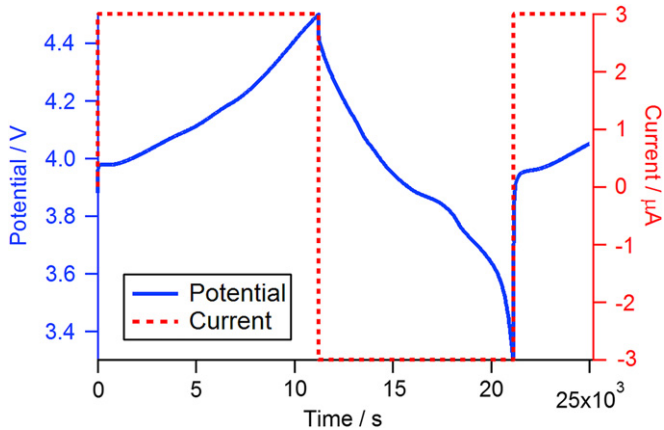

Fig. 7. Voltage profiles of Li/LiCoO$_2$ from a thin film cell. The cell was cycled between 3.0 and 4.5 V at a current of 3 μA.

than in the Swagelok case. Also, the absence of an external pressure to maintain electrode–current collector contact in the fluid cell may also increase the contact resistance of the sample. Thus, under the assumption that the starting points of the simulation are the same with each measurement, the relative height changes from the starting point are compared. While scanning, the applied voltage continued to increase, so the middle value of the voltage during each scan is represented in the resultant figures and compared with the simulation results.

As can be seen in Fig. 8, in the case of pillar no. 3, both the height changes calculated in the simulation and those found by experimental measurement show similar trends. The measured height changes were found to gradually increase to about 26 nm, while the simulation calculated a change of 22 nm at the end of charge (4.15 V). This volume expansion is caused by the removal of the Li-ions, which causes adjacent CoO$_2$ layers to undergo increased electrostatic repulsions as negatively charged oxygen–oxygen
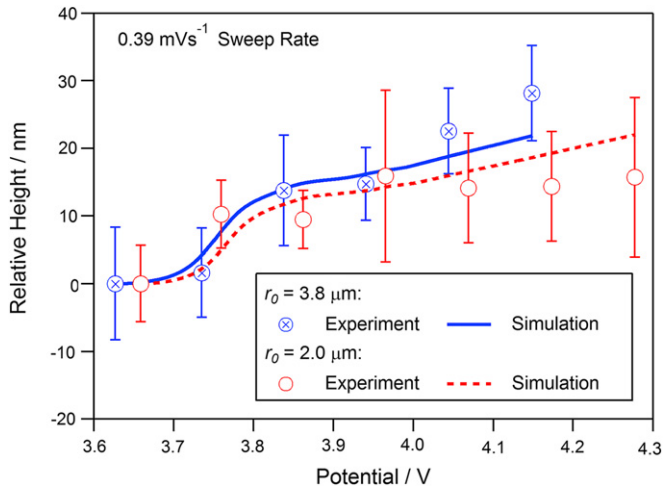

Fig. 8. The height evolution of pillar no. 3 ($r_0 = 3.8$ μm) and no. 2 ($r_0 = 2.05$ μm) when the cell was swept with 0.39 mV s^{-1}. The mean value of the height over 340 nm × 340 nm as measured experimentally is represented by markers, and the vertical bar represents the surface roughness as one standard deviation from the mean. The solid line shows the simulation result. The solid blue line represents the simulation results on pillar no. 3, while the dotted red line represents the simulation results on pillar no. 2. The blue circle bar marked 'x' indicates the measurement results on pillar no. 3, and the unmarked red circle bar indicates the measurement results on pillar no. 2. (For interpretation of the references to color in this figure legend, the reader is referred to the web version of this article.)

interactions increase. It is worth noting that the abrupt increases of the OCV in the low voltage regions result in slow increases in the height of the sample because of low current flow. However, as it passes the plateau region of the OCV, the flux of Li ions becomes increased, even at constant voltage sweep rates, and as a result, the height increases quickly. The volume increases by about 1.3%, which is lower than the 2.4% expansion in c_{hex} from $LiCoO_2$ to in $Li_{0.49}CoO_2$. This is because the grain size in the sample is 50–70 nm, which is very small compared to the pillar size. Thus, the volume expansion can be considered isotropic, as we assumed in the simulations.

Fig. 8 also shows results obtained from the small pillar (pillar no. 2 in Fig. 1, $r_0 = 2.05$ μm). Similar to the case of the larger pillar (pillar no. 3 in Fig. 1, $r_0 = 3.8$ μm), the simulation results follow the measurement very closely. However, here the maximum height change is smaller than in the case of the larger pillar. The height increase comes from volume expansion resulting from electrostatic repulsion. It implies that a larger pillar will exhibit a larger height change. The effect of pillar size on the deintercalation-induced vertical displacement is demonstrated in Fig. 9, where the height change as a function of potential is compared for the two pillars with different radii. It can be seen that during the initial stages, at the same current, the height change in the smaller pillar is larger because Li-ion extraction occurs not only from the surface but from the inner portion of the pillar as well; this is due to the smaller size of the pillar. In contrast, in the larger pillar, Li-ions are extracted from the surface, resulting in lower expansion. As the cell is charged further, however, the larger pillar also experiences similar deintercalation at its interior, resulting in greater height change.

The sweep rate is another important factor in determining strain and stress due to intercalation because it determines the Li-ion concentration distribution inside the particle. The current density at the surface of a particle inside a cell may vary depending on the C-rate and also on the location of the particle in the electrode; the current density is higher for particles near the separator (electrode surface). To elucidate the influence of the sweep rate on the volume strain level, the sweep rate was increased by a factor of two. Contamination from the side reactions and gas generation resulted in a low quality AFM image. Therefore, the discussion of the de-lithiation rate effect is based on the results of simulations (Fig. 10). The measured global height changes at the higher sweep rate are smaller than those measured at the lower sweep rate. As the sweep rate increases, the total amount of Li-ion extracted from the particle decreases so that the volume expansion also decreases. However, a higher current density may induce a higher gradient in
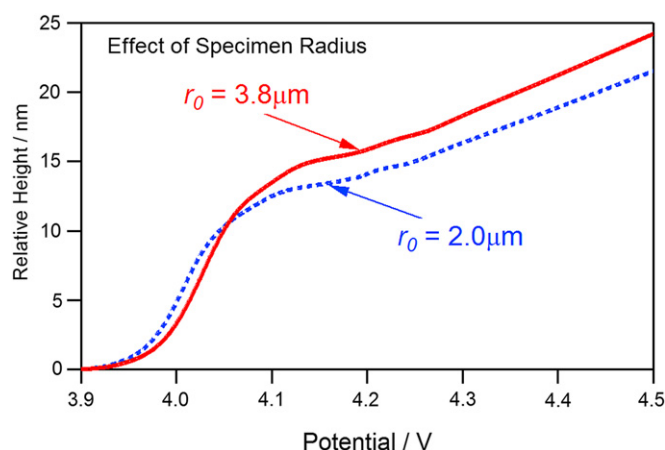

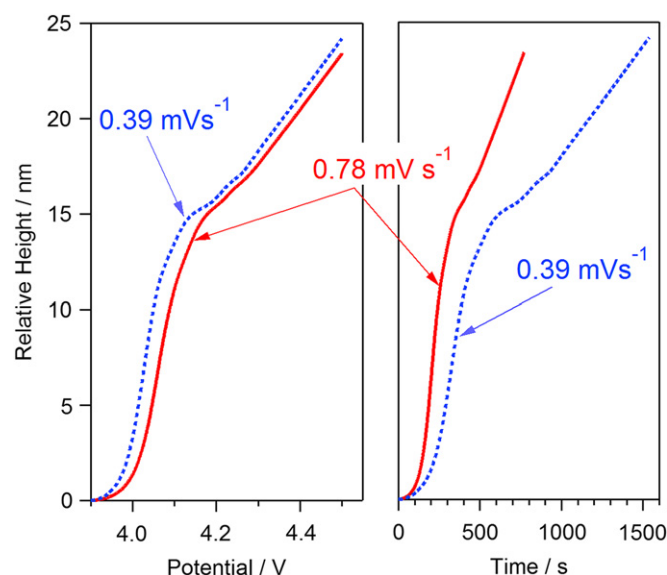Fig. 10. The numerical results of the sweep rate effect on height evolution. The cell was swept with 0.39 mV s⁻¹ and 0.78 mV s⁻¹ rates.

the lithium concentration, as can be seen in the results of a numerical simulation shown in Fig. 11. Here, pillar no. 3 was swept with different sweep rates (a) 0.39 mV s⁻¹ (b) 0.78 mV s⁻¹. This high gradient can lead to a higher stress level. Also, a high discharge rate may cause an unintended over-discharge, which may lead to degradation of the cell; if the current is sufficiently high, the state of charge (SOC) of the material could exceed $x = 1$ at the sharp surface of particles in the electrode.

Numerical modeling is an advantageous approach for evaluating the effect of the different operating conditions on strain and stress levels, whereas it is not easy to measure stress level via an AFM experiment. The current modeling results are consistent with measurement results in principle. This implies that numerical results can provide further information than was measured. Fig. 12(a) shows the calculated displacement in the z direction and Fig. 12(b) shows total displacement in pillar no. 3 when it was swept with 0.39 mV s⁻¹ rate. The deformation is exaggerated 100 times to show the shape change. Due to the unconstrained boundary condition and lower Li-ion concentration around the outer surface, the specimen expands further at the outer surface. Consequently, the pillar shape is convex. This convex shape is also verified from the measurements shown in Fig. 13 for pillar no. 3. The average height is decreased as the radial position is increased.

Yield stress and von Mises stress are not proper failure criteria for brittle materials. Also, the compressive strengths for ceramics are much larger than the ultimate tensile strength. The maximum tensile stress is appropriate information in predicting fracture
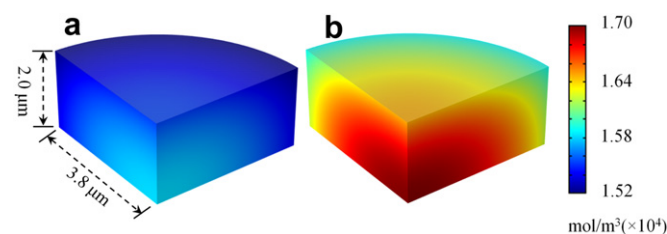

Fig. 9. The numerical results of the micro-pillar size effect on height evolution. The cells were swept with 0.39 mV s⁻¹ rate.

Fig. 11. The lithium concentration profile in pillar no. 3 when the potential is 4.15 V with different sweep rates: (a) 0.39 mV s⁻¹ (b) 0.78 mV s⁻¹.

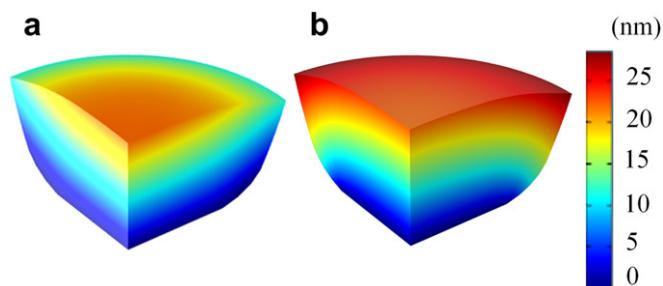**Fig. 12.** Exaggerated deformation of pillar no. 3 where the color map represents (a) z-displacement (b) total displacement.

Fig. 14. Mechanical boundary condition effects with different sweep rate on the maximum principal stresses in pillar no. 3.

failure of brittle materials. The maximum principal stress occurs at the center of the micro-pillar due to expansion of the specimen. Fig. 14 shows the computed maximum principal stress in the micro-pillar as a function of potential for different sweep rates and different applied boundary conditions. As the cell is charged, the maximum stress increases to around 217 MPa when the voltage is 4.3 V and the boundary of the bottom of the pillar is fixed. However, if this boundary condition is changed to a roller condition (unconstrained in the $x–y$ plane, but with zero displacement prescribed in the z-direction), the stress level is decreased to 35 MPa. This is attributed to a relaxation of the strain by allowing free movement in the horizontal plane. For the same reason, the vertical displacement is larger with a fixed boundary condition. Similarly, the current density effects are different depending on the boundary condition. For a roller boundary condition, higher current density indicates a higher stress level. However, for the fixed boundary condition, the stress level is not changed significantly, and a lower sweep rate results in a slightly higher level. This is attributed to a relaxation in the roller boundary condition, so the concentration gradient is more critical than the actual Li-concentration. This can also explain why the maximum stress level occurs during the charge process where the concentration gradient is maximized. However, in the fixed boundary condition, there is no relaxation phenomenon, which means that as Li-ions are extracted further, there is more volume expansion. This causes the monotonous increase in stress level in the time profile.

The deviation in the measured height change from the simulation may result from many different factors in addition to the
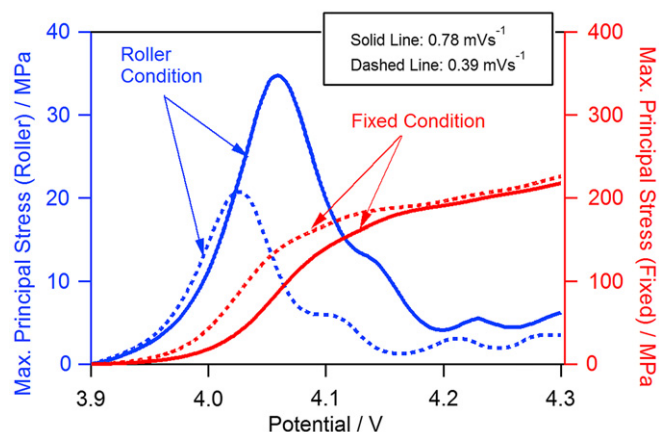

Fig. 13. Comparison between experimentally measured results and those predicted by simulation based on cross-sectional profiles of the micro-machined pillar no. 3 after de-lithiation.

intrinsic measurement error associated with the instrumentation and technique. LiCoO$_2$ is known to dissolve into the electrolyte, which may impact the measured heights of the electrode; weights of dissolved metal ions measured by Atomic Absorption Spectroscopy (AAS) have been reported for LiCoO$_2$ as 0.8% of the sample weight [44]. Also, the adhesion of the active material to the substrate may become worse. This phenomenon was observed in a different sample. After continuous scanning in contact mode with a Si$_3$N$_4$ tip, fracture occurred at the point of attachment of the micro-machined pillar to the current collector. Adhesion between the gold substrate and the LiCoO$_2$ film was not sufficient to endure continuous force exertion. Also, as there was gas generation during cycling, the resultant bubbles hindered scanning and prevented obtaining good images. In addition, the AFM probe shielding effect may have changed the Li-ion content over the pillar sample. Another characteristic feature of LiCoO$_2$ that might have affected the results is phase transition; X-ray diffraction examinations have indicated that a two phase region can be generated between $x = 0.75$ and $x = 0.975$ for a Li$_x$CoO$_2$ electrode [14].

5. Conclusions

This work used a scanning probe technique to understand dynamic deformation processes during Li deintercalation in a Li$_x$CoO$_2$ cathode material. A unique experimental approach with a pre-defined micro-machined specimen has allowed for *in situ* characterization of morphology of the specimen. The dimensional changes of FIB micro-machined samples were monitored *in situ*, and the results showed expansion in volume due to electrostatic repulsion. The volume expansions are generally in good agreement with previous XRD measurements. The averaged height increase calculated from XRD measurements of volume expansion is about 1.34% when x is changed from 1 to 0.35 in Li$_x$CoO$_2$, while the measurement from this *in situ* AFM experiment is about 1.28–1.3%. The results of the modeling follow the experimental results rather well. The changes in volume expansion due to the geometry and kinetic rate changes showed the same trend with our simulation results—a steep expansion in plateau OCV regions and a larger expansion for the larger pillar. The computed profile of the deformed by de-lithiation micro-pillar matches well with the experimentally measured shape changes in the specimen. Further, the simulation results, validated from measurements, provided the stress state, which can be used in assessing the structural stability of the material but is not easily measured.
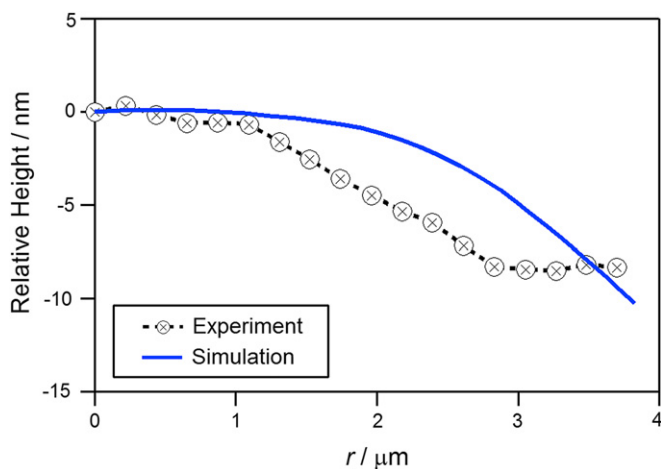
Acknowledgments

References

[1] R. Koksbang, J. Barker, H. Shi, W.Y. Saïdi, Solid State Ionics 84 (1996) 1.
[2] Y. Zhang, C.-Y. Wang, Journal of the Electrochemical Society 156 (2009) A527.
[3] I.D. Scott, Y.S. Jung, A.S. Cavanagh, Y. Yan, A.C. Dillon, S.M. George, S.-H. Less, Nano Letters 11 (2011) 414.
[4] J.B. Bates, N.J. Dudney, D.C. Lubben, G.R. Gruzalski, B.S. Kwak, X. Yu, R.A. Zuhr, Journal of Power Sources 54 (1995) 58.
[5] J.D. Perkins, C.S. Bahn, P.A. Parilla, J.M. McGraw, M.L. Fu, M. Duncan, H. Yu, D.S. Ginley, Journal of Power Sources 81–82 (1999) 675.
[6] B. Wang, J.B. Bates, F.X. Hart, B.C. Sales, R.A. Zuhr, J.D. Robertson, Journal of the Electrochemical Society 143 (1996) 3203.
[7] K. Yamada, N. Sato, T. Fujino, C.G. Lee, I. Uchida, J.R. Selman, Journal of Solid State Electrochemistry 3 (1999) 148.
[8] C.-L. Wang, Y.C. Liao, F.C. Hsu, N.H. Tai, M.K. Wu, Journal of the Electrochemical Society 152 (2005) A653.
[9] M.K. Kim, H.T. Chung, Y.J. Park, J.G. Kim, J.T. Son, K.S. Park, H.G. Kim, Journal of Power Sources 99 (2001) 34.
[10] K.H. Hwang, S.H. Lee, S.K. Joo, Journal of Power Sources 54 (1995) 224.
[11] H.J. Orman, P.J. Wiseman, Acta Crystallographica Section C − Crystal Structure Communications 40 (1984) 12.
[12] K. Mizushima, P.C. Jones, P.J. Wiseman, J.B. Goodenough, Materials Research Bulletin 15 (1980) 783.
[13] J.N. Reimers, J.R. Dahn, Journal of the Electrochemical Society 139 (1992) 2091.
[14] T. Ohzuku, A. Ueda, Journal of the Electrochemical Society 141 (1994) 2972.
[15] G.G. Amatucci, J.M. Tarascon, L.C. Klein, Solid State Ionics 83 (1996) 167.
[16] H.F. Wang, Y.I. Jang, B.Y. Huang, D.R. Sadoway, Y.T. Chiang, Journal of the Electrochemical Society 146 (1999) 473.
[17] H. Gabrisch, R. Yazami, B. Fultz, Electrochemical and Solid State Letters 5 (2002) A111.
[18] K. Rhodes, N. Dudney, E. Lara-Curzio, C. Daniel, Journal of the Electrochemical Society 157 (2010) A1354.
[19] M. Qu, W.H. Woodford, J.M. Maloney, W.C. Carter, Y.-M. Chiang, K.J. Van Vliet, Advanced Energy Materials (2012).
[20] W.H. Woodford, W.C. Carter, Y.-M. Chiang, Energy & Environmental Science 5 (2012) 8014.
[21] K. Rhodes, R. Meisner, Y. Kim, N. Dudney, C. Daniel, Journal of the Electrochemical Society 158 (2011) A890.
[22] M. Balasubramanian, X. Sun, X.Q. Yang, J. McBreen, Journal of Power Sources 92 (2001) 1.
[23] V.R. Albertini, P. Perfetti, F. Ronci, P. Reale, B. Scrosati, Applied Physics Letters 79 (2001) 27.
[24] L.Y. Beaulieu, V.K. Cumyn, K.W. Eberman, L.J. Krause, J.R. Dahn, Review of Scientific Instruments 72 (2001) 3313.
[25] N. Balke, S. Jesse, Y. Kim, L. Adamczyk, I.N. Ivanov, N.J. Dudney, S.V. Kalinin, ACS Nano 4 (2010) 7349.
[26] S. Guo, S. Jesse, S. Kalnaus, N. Balke, C. Daniel, S.V. Kalinin, Journal of the Electrochemical Society 158 (2011) A982.
[27] A. Clemencon, A.T. Appapillai, S. Kumar, Y. Shao-Horn, Electrochimica Acta 52 (2007) 4572.
[28] J. Nanda, J.T. Remillard, A. O'Neil, D. Bernardi, T. Ro, K. Nietering, T.J. Miller, Advanced Functional Materials 21 (2011) 3282.
[29] S. Prussin, Journal of the Electrochemical Society 108 (1961) C213.
[30] X.C. Zhang, W. Shyy, A.M. Sastry, Journal of the Electrochemical Society 154 (2007) A910.
[31] X.C. Zhang, A.M. Sastry, W. Shyy, Journal of the Electrochemical Society 155 (2008) A542.
[32] J. Park, W. Lu, A.M. Sastry, Journal of the Electrochemical Society 158 (2011) A201.
[33] Y.T. Cheng, M.W. Verbrugge, Journal of Applied Physics 104 (2008).
[34] Y.T. Cheng, M.W. Verbrugge, Journal of the Electrochemical Society 157 (2010) A508.
[35] S. Kalnaus, K. Rhodes, C. Daniel, Journal of Power Sources 196 (2011) 8116.
[36] J. Christensen, J. Newman, Journal of the Electrochemical Society 153 (2006) A1019.
[37] J. Christensen, J. Newman, Journal of Solid State Electrochemistry 10 (2006) 293.
[38] S. Renganathan, G. Sikha, S. Santhanagopalan, R.E. White, Journal of the Electrochemical Society 157 (2010) A155.
[39] W.H. Woodford, Y.M. Chiang, W.C. Carter, Journal of the Electrochemical Society 157 (2010) A1052.
[40] M. Zhu, J. Park, A.M. Sastry, Journal of the Electrochemical Society 159 (2012) A492.
[41] D. Zhang, B.N. Popov, R.E. White, Journal of the Electrochemical Society 147 (2000) 831.
[42] J. Akimoto, Y. Gotoh, Y. Oosawa, Journal of Solid State Chemistry 141 (1998) 298.
[43] H. Orman, P. Wiseman, Acta Crystallographica 40 (1984) 12.
[44] W. Choi, A. Manthiram, Journal of the Electrochemical Society 153 (2006) A1760.
[45] R.J. Gummow, D.C. Liles, M.M. Thackeray, Materials Research Bulletin 28 (1993) 235.
[46] M. Holzapfel, C. Haak, A. Ott, Journal of Solid State Chemistry 156 (2001) 470.
[47] Y. Takahashi, N. Kijima, K. Dokko, M. Nishizawa, I. Uchida, J. Akimoto, Journal of Solid State Chemistry 180 (2007) 313.
[48] J.T. Hertz, Q. Huang, T. McQueen, T. Klimczuk, J.W.G. Bos, L. Viciu, R.J. Cava, Physical Review B 77 (2008).
[49] M. Pollet, M. Blangero, J.P. Doumerc, R. Decourt, D. Carlier, C. Denage, C. Delmas, Inorganic Chemistry 48 (2009) 9671.
[50] M. Doyle, J. Newman, A.S. Gozdz, C.N. Schmutz, J.M. Tarascon, Journal of the Electrochemical Society 143 (1996) 1890.
[51] C.W. Wang, A.M. Sastry, Journal of the Electrochemical Society 154 (2007) A1035.